Chemical Science

ROYAL SOCIETY OF CHEMISTRY

EDGE ARTICLE

View Article Online
View Journal | View Issue

Open Access Article. Published on 27 January 2025. Downloaded on 11/2/2025 12:12:14 PM.
This article is licensed under a Creative Commons Attribution-NonCommercial 3.0 Unported Licence.

Check for updates

Cite this: *Chem. Sci.*, 2025, **16**, 3646

All publication charges for this article have been paid for by the Royal Society of Chemistry

Co^{II}-organic 'soft' metallo-supramolecular polymer nanofibers for efficient photoreduction of CO_2†

Souvik Mondal,[a] Faruk Ahamed Rahimi,[a] Tarak Nath Das,[b] Sukhendu Nath[cd] and Tapas Kumar Maji*[ab]

Coordination-driven metallo-supramolecular polymers hold significant potential as highly efficient catalysts for photocatalytic CO_2 reduction, owing to the covalent integration of the light harvesting unit, catalytic center and intrinsic hierarchical nanostructures. In this study, we present the synthesis, characterization, and gelation behaviour of a novel low molecular weight gelator (LMWG) integrating a benzo[1,2-*b*:4,5-*b*′]dithiophene core with terpyridine (TPY) units *via* alkyl amide chains (TPY-BDT). The two TPY ends of the TPY-BDT unit efficiently chelate with metal ions, enabling the formation of a metallo-supramolecular polymer that brings together the catalytic center and a photosensitizer in close proximity, maximizing catalytic efficiency for CO_2 reduction. The self-assembly of TPY-BDT with Co^{II} ions yields a Co-TPY-BDT coordination polymer gel (CPG) with a 3D interconnected fibrous morphology, facilitating rapid electron transfer and efficient substrate diffusion. The Co-TPY-BDT CPG achieves an outstanding CO_2 to CO conversion, producing 33.74 mmol g^{-1} of CO in 18 hours with ~99% selectivity under visible light irradiation, using triethylamine (TEA) as a sacrificial electron donor. Remarkably, the Co-TPY-BDT CPG demonstrates significant catalytic activity even under low-concentration CO_2 atmospheres (5% CO_2, 95% Ar), producing 1.9 mmol g^{-1} of CO in 10 hours with a selectivity of 94.6%. Moreover, *In situ* diffuse reflectance Fourier transform (DRIFT) study, femtosecond transient absorption spectroscopy, and DFT calculations were employed to elucidate the CO_2 to CO reaction mechanism.

Received 31st December 2024
Accepted 15th January 2025

DOI: 10.1039/d4sc08814j

rsc.li/chemical-science

Introduction

The rapid advancement of industrialization and the continuous rise in carbon emissions have intensified the conflict between growing energy demands and sustainable development.[1–5] One promising solution to this issue is CO_2 conversion, which allows for the reutilization of exhaust gases and the production of valuable fuels.[6,7] Inspired by nature's photosynthesis process, researchers are exploring ways to use sunlight to convert CO_2 into fuels or high-value-added chemicals.[8,9] A central goal in this field is to develop systems that are capable of efficiently and selectively catalysing CO_2 reduction under visible light irradiation, positioning photocatalysis as one of the key technologies in the pursuit of an energy-sustainable society. Recently, various catalysts have been developed for the photocatalytic CO_2 reduction reaction (CO_2RR), including metal oxides,[10–12] g-C_3N_4-based photocatalysts,[13] metal–organic frameworks (MOFs),[9,14–16] and covalent organic frameworks (COFs).[17–20] Moreover, significant progress has also been made in achieving high CO_2 photoreduction activity using soft hybrid nanomaterials due to their advantageous nanostructures.[21–23]

Coordination polymer gels (CPGs) represent a novel class of 'soft' hybrid nanomaterials formed through the self-assembly of low molecular weight gelators (LMWGs) with metal ions.[21,22,24,25] These CPGs establish extensive networks where metal–LMWG interactions guide the precise formation of diverse nanostructures, including fibers, tubes, rings, ribbons, and vesicles.[24,26] Reinforced by π–π stacking and hydrogen bonding, these structures exhibit exceptional stability and uniformity.[24,27] The fibrous morphology offers a large surface area and the interconnected network enhances reactant diffusion and electron transfer, which is particularly advantageous for boosting efficiency in photocatalysis.[28–30] The presence of metal centers in CPGs has attracted significant attention for diverse applications in optics, catalysis, redox reactions, and magnetism.[24,31,32] In our approach, we have developed a novel LMWG-based linker to harness solar energy for CO_2 reduction to produce solar fuel.

[a]*Chemistry and Physics of Materials Unit, School of Advanced Materials (SAMat), Jawaharlal Nehru Centre for Advanced Scientific Research, Jakkur, Bangalore 560064, India. E-mail: tmaji@jncasr.ac.in; Web: https://www.jncasr.ac.in/faculty/tmaji*

[b]*New Chemistry Unit, School of Advanced Materials (SAMat), Jawaharlal Nehru Centre for Advanced Scientific Research, Jakkur, Bangalore 560064, India*

[c]*Radiation and Photochemistry Division, Bhabha Atomic Research Center, Mumbai 400085, India*

[d]*Homi Bhabha National Institute, Anushaktinagar, Mumbai 400094, India*

† Electronic supplementary information (ESI) available. See DOI: https://doi.org/10.1039/d4sc08814j

© 2025 The Author(s). Published by the Royal Society of Chemistry

Open Access Article. Published on 27 January 2025. Downloaded on 11/2/2025 12:12:14 PM.
This article is licensed under a Creative Commons Attribution-NonCommercial 3.0 Unported Licence.

Achieving the integration and assembly of all essential functional molecular components into a robust artificial system for photocatalysis remains a pivotal long-term scientific goal. In this work, we present a strategy for fabricating CPG-based soft materials as highly efficient photocatalysts for CO_2 reduction, achieved by integrating a compatible low molecular weight gelator (LMWG) as a light-harvesting component with a redox-active metal ion as the catalytic center.[21,22] In our LMWG design, we have chosen a π-conjugated benzo[1,2-*b*:4,5-*b*′] dithiophene (BDT) chromophore as a light-harvesting unit for its structural symmetry and rigid large aromatic π-backbone, which enhances electron delocalization and charge transport.[33–35] The BDT core was further modified by attaching two terpyridine moieties *via* the alkyl amide chain.[36] This functionalization enables additional metal binding, thereby creating catalytic sites for CO_2 reduction. Utilizing cobalt bis(terpyridine)-based complexes as the catalytic center provides the system with stable redox states and a high affinity for CO_2 binding, making it highly effective for photocatalytic applications.[37,38]

Herein, we developed a coordination polymer gel (CPG) by self-assembling a bipodal terpyridyl-BDT-based LMWG (TPY-BDT) with $CoCl_2 \cdot 6H_2O$. The resulting Co-TPY-BDT CPG, with interconnected fibrous morphology, showed exceptional photocatalytic CO_2 reduction capability using triethylamine (TEA) as a sacrificial agent (Scheme 1). It achieved 33.74 mmol g^{-1} of CO in 18 h with an outstanding selectivity of ∼99%. Furthermore, the Co-TPY-BDT CPG demonstrated excellent activity in reducing low-concentration CO_2 (5% CO_2, 95% Ar), yielding 1.9 mmol g^{-1} of CO in 10 h with a very good selectivity of 94.6%. To the best of our knowledge, this soft hybrid material shows one of the best photocatalytic activities using both pure CO_2 and low-concentration CO_2. In this system, the BDT core functions as the light-harvesting unit, while the $[Co(TPY)_2]^{2+}$ complex acts as the catalytic center. Comprehensive investigations, including *in situ* DRIFT studies, femtosecond transient absorption (fsTA) spectroscopy, and DFT calculations, provide valuable insights into the plausible mechanism underlying the CO_2 reduction process facilitated by this innovative CPG–based catalyst under visible light.

Results and discussion

The TPY-BDT LMWG was synthesized *via* amide coupling of 2,2′:6′,2″-terpyridin-4′-yl-propane-1,3-diamine (TPY-NH_2) and benzo[1,2-*b*:4,5-*b*′]dithiophene-2,6-dicarboxylic acid (BDT$(COOH)_2$) and characterized using ^{1}H-NMR and MALDI (Fig. S1–S3†) spectrometry. UV-Vis analysis of TPY-BDT in DMSO (10^{-4} M) revealed a distinct absorption band at 280 nm, corresponding to the π→π* transition of the TPY unit.[21,22] Additionally, the spectrum revealed distinct bands at 327 nm and 376 nm, characteristic of the π→π* transitions associated with the BDT core.[39–42] The photoluminescence spectrum of TPY-BDT displayed emission ranging from 400 nm to 500 nm, with a maximum at 412 nm when excited at 380 nm (Fig. S4†). Featuring π electron-rich BDT cores and amide groups, TPY-BDT has the ability to self-assemble *via* π–π stacking and hydrogen bonding interactions in an appropriate solvent environment. Hence, we explored the gelation propensity of the TPY-BDT LMWG in various solvent compositions (Table S1†). A mixture of TPY-BDT (0.006 mmol), dimethyl sulfoxide (DMSO) (200 μl), and water (H_2O) (100 μl) was heated to 60 °C for 20 minutes, yielding a viscous solution. Upon subsequent cooling at room temperature for 1 h, an organogel formed (Fig. 1A), verified through the inversion test method as well as the rheology experiment. In the rheology experiment employing the amplitude sweep method (strain range from 0.001% to 100%) for the organogel (TPY-BDT OG), the storage modulus (G') surpassed the loss modulus (G'') within the lower strain range (0.01% to 10%), indicating the stable viscoelastic nature of the material and confirming gel formation (Fig. 1C). TPY-BDT OG was dried under vacuum at 60 °C for 12 h to obtain the xerogel. TPY-BDT OG was characterized by Fourier transform infrared (FT-IR) spectroscopy, displaying a characteristic amide –C=O vibration at 1610 cm^{-1} and amide –N–H stretching bands at 3348 cm^{-1}, confirming the presence of the –$CONH_2$ group

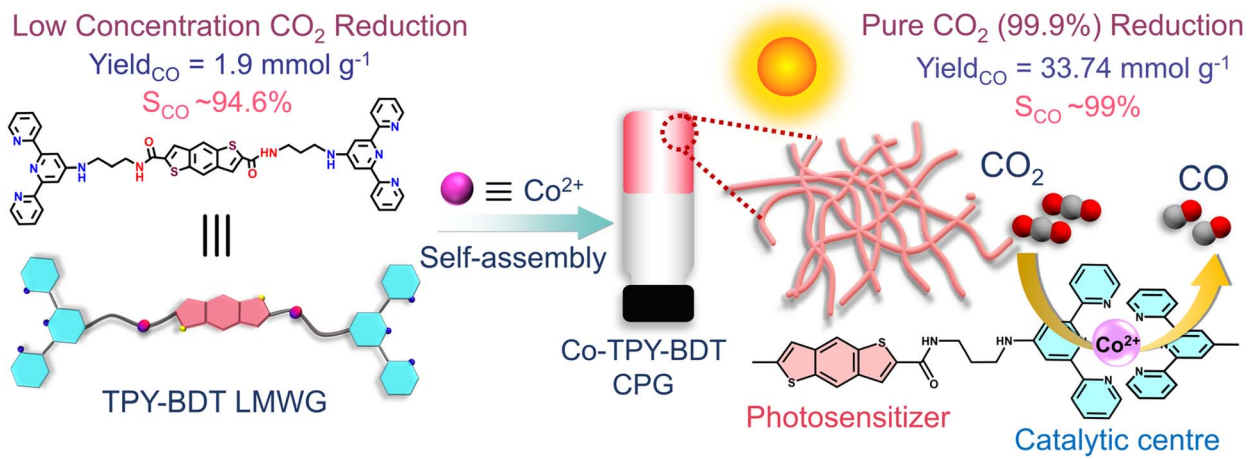

Scheme 1 Schematic showing the self-assembly of the TPY-BDT LMWG with Co^{II} to generate Co-TPY-BDT CPG with nanofiber morphology towards photocatalytic CO_2 reduction using pure CO_2 and low concentration CO_2.

Open Access Article. Published on 27 January 2025. Downloaded on 11/2/2025 12:12:14 PM.
This article is licensed under a Creative Commons Attribution-NonCommercial 3.0 Unported Licence.

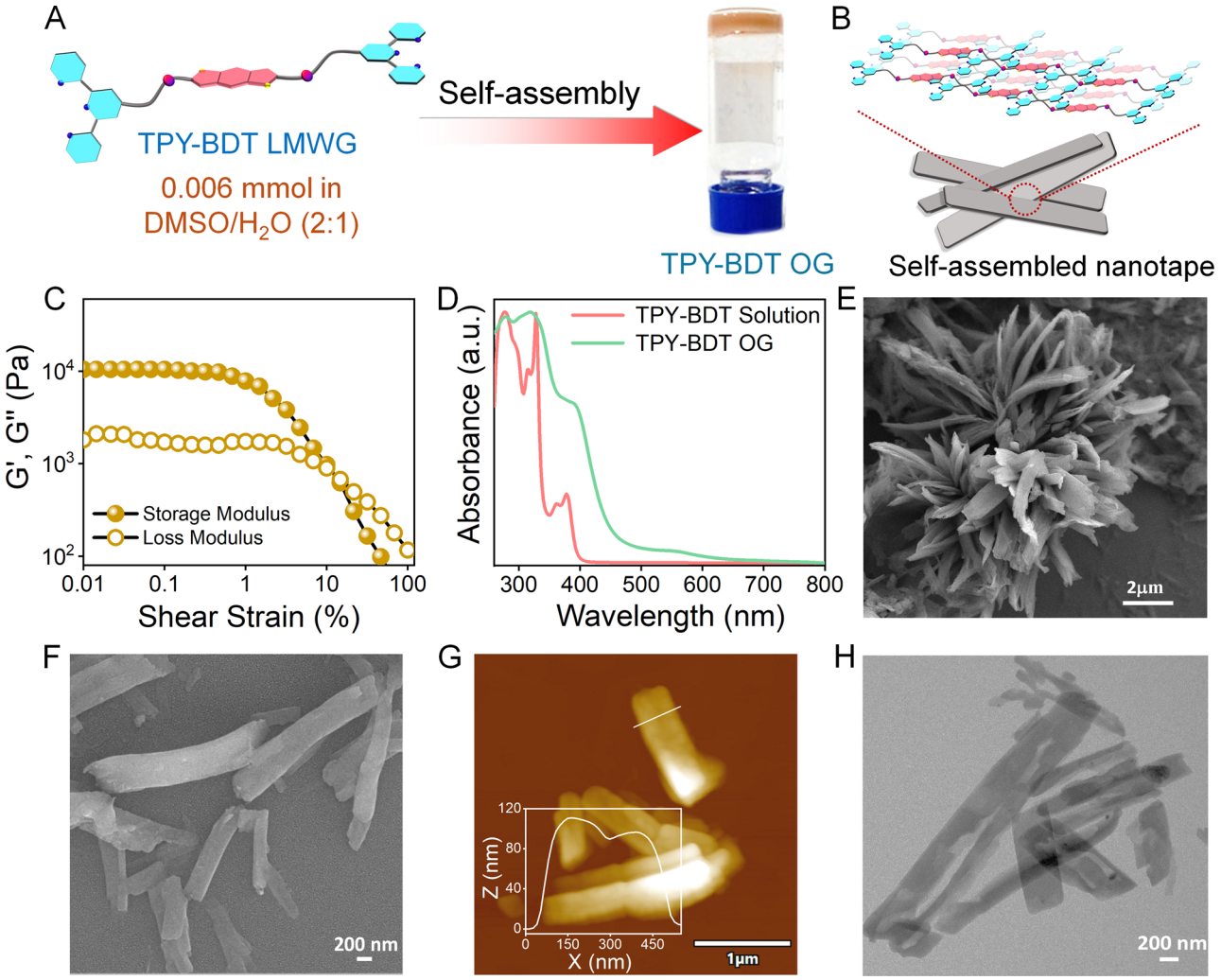

Fig. 1 (A) Schematic of the TPY-BDT LMWG towards the formation OG. (B) Schematic of the self-assembled nanotape morphology. (C) Strain sweep rheology measurement of TPY-BDT OG. (D) Comparison of absorption spectra of the TPY-BDT LMWG in solution with TPY-BDT OG in the xerogel state. (E and F) FESEM, (G) AFM, and (H) TEM images of TPY-BDT OG showing nanotape like morphology.

(Fig. S5†).[22] The UV-Vis absorption analysis of TPY-BDT OG revealed slightly red-shifted bands at 320 and 410 nm compared to the monomeric form, which can be ascribed to the aggregation of the BDT core in the gel state (Fig. 1D). Additionally, a weak broad absorption band with a maximum at ~556 nm was also observed in the absorption spectrum of TPY-BDT OG.[22] TDDFT calculations for TPY-BDT OG were performed considering the TPY-BDT unit, which revealed a theoretical absorption band at 384.22 nm corresponding to an experimental band at 410 nm. The 410 nm band arises due to a transition from the highest occupied molecular orbital (HOMO) on the BDT core to the lowest unoccupied molecular orbital (LUMO) delocalized through the BDT(CONH—)$_2$ unit of TPY-BDT OG (Fig. S6 and Table S2†). The optical bandgap was determined to be 2.80 eV using the Tauc plot (Fig. S7a†). The emission study of TPY-BDT OG revealed a broad emission band with a maximum at ~470 nm (λ_{ex} = 380 nm) (Fig. 2E). Morphological analysis of TPY-BDT OG using field emission scanning electron microscopy (FE-SEM) (Fig. 1E and F), atomic force microscopy (AFM) (Fig. 1G) and transmission electron microscopy (TEM) (Fig. 1H) revealed a flower-like architecture formed by the assembly of 1D nanotapes (Fig. 1B). From AFM analysis, the height of the thinnest nanotape was found to be around 100 nm, while its width and average length were determined to be approximately 400–500 nm and 1.0–1.3 μm, respectively (Fig. 1G).

Next, we aim to synthesize a coordination polymer gel (CPG) by combining the TPY-BDT LMWG, which contains two metal-binding terpyridine units, with appropriate metal ions. We opted for Co^{II} as the metal node to coordinate with TPY, as it facilitates easy electron–hole separation owing to its stable redox states.[43,44] To obtain the stoichiometric ratio of the complexation, UV-Vis titration of TPY-BDT (5×10^{-5} M in DMSO) with $CoCl_2 \cdot 6H_2O$ (5×10^{-3} M in H_2O) was performed (Fig. 2A). A new absorption band appeared during the titration at 303 nm and 313 nm with an increment in the intensity. This suggested Co^{II} binding to the TPY center, and the isosbestic point analysis showed the complexation between TPY-BDT with the Co^{II} ion completed at a ratio of 1 : 1 at the saturation point (Fig. S8a†). The association constant (K_a) for the Co^{II} ion binding with TPY-BDT was determined from the Benesi–Hildebrand plot and

 © 2025 The Author(s). Published by the Royal Society of Chemistry

Open Access Article. Published on 27 January 2025. Downloaded on 11/2/2025 12:12:14 PM.
This article is licensed under a Creative Commons Attribution-NonCommercial 3.0 Unported Licence.

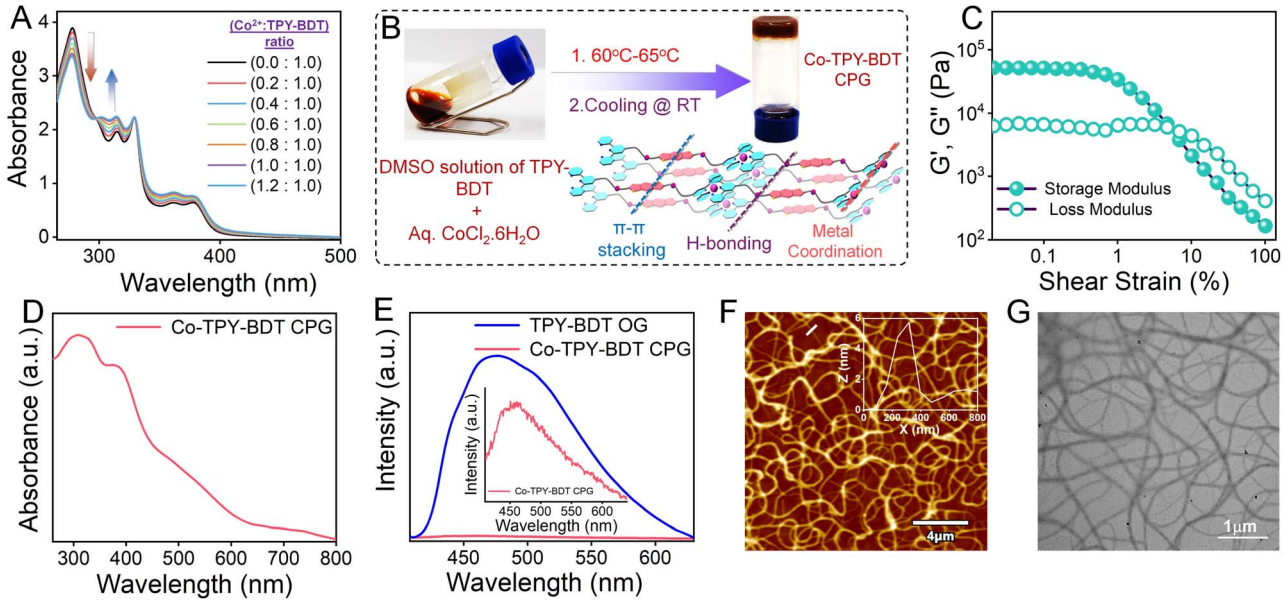

Fig. 2 (A) UV-Visible titration of the TPY-BDT LMWG with Co^{II} ions. (B) Gelation of Co-TPY-BDT CPG. (C) Strain sweep rheology measurement of Co-TPY-BDT CPG. (D) Absorption spectrum and (E) emission spectra (λex = 380 nm) of Co-TPY-BDT CPG and TPY-BDT OG. (F) AFM image of Co-TPY-BDT CPG (inset: the height profile of fiber). (G) TEM image of Co-TPY-BDT CPG.

calculated to be 2.84×10^4 M^{-1} (Fig. S8b†). Therefore, the CPG was prepared with a 1 : 1 molar ratio of TPY-BDT and Co^{II} metal ions. A dropwise addition of an aqueous solution of $CoCl_2 \cdot 6H_2O$ (0.006 mmol, 100 μl) into a TPY-BDT solution (0.006 mmol) in DMSO (200 μl) was carried out under heating at 60 °C, followed by cooling to room temperature for 1 h, yielding a dark brown gel (Co-TPY-BDT CPG) (Fig. 2B). The gel formation was confirmed by the inversion test as well as by rheology measurement like OG. The storage modulus (G') exhibited values approximately 10 times higher than the loss modulus (G'') within a lower strain range (0.001 to 10%), suggesting the stable viscoelastic nature of the Co-TPY-BDT CPG (Fig. 2C). Co-TPY-BDT CPG exhibited an approximately 5-fold higher G' value compared to TPY-BDT OG, potentially attributed to the coordination of the Co^{II} ion.[45] The CPG was dried under vacuum at 60 °C for 12 h to obtain the xerogel. The FT-IR spectrum of Co-TPY-BDT CPG exhibited a characteristic amide –C═O vibration at 1620 cm^{-1} and amide –N–H stretching band at 3245 cm^{-1}, confirming the presence of the $-CONH_2$ group in the Co-TPY-BDT CPG (Fig. S9†).[22,46] The UV-Vis absorption spectrum of Co-TPY-BDT CPG in the xerogel state resembled that of TPY-BDT OG. An additional broad absorption band was observed between 450 and 600 nm, which is attributed to both the d–d transition and MLCT of the low spin $[Co(TPY)_2]^{2+}$ unit in the Co-TPY-BDT CPG (Fig. 2D and S10†).[38,47] The significant emission quenching in Co-TPY-BDT CPG compared to TPY-BDT OG can be attributed to self-absorption or excited state electron transfer from the BDT core to the $[Co^{II}(TPY)_2]^{2+}$ within the CPG (Fig. 2E). The morphology of the Co-TPY-BDT CPG was investigated by AFM (Fig. 2F), TEM (Fig. 2G) and FE-SEM (Fig. S11†). These analyses revealed interconnected fiber morphology of the CPG. The AFM images of the CPG showed that the single fiber has a minimum height of ∼9 nm and a minimum width of around ∼300 nm (Fig. 2F). Additionally, the DRS spectrum of Co-TPY-BDT CPG revealed an optical band gap of 1.89 eV, which is smaller than the band gap of TPY-BDT OG (Fig. S7b†). We measured the photoluminescence (PL) lifetime using the time-correlated single-photon counting (TCSPC) method. The Co-TPY-BDT CPG exhibited a notably lower lifetime of 1.06 ns in comparison to the TPY-BDT OG, which showed a lifetime of 4.64 ns (Fig. S12 and Table S3†). This decrease in lifetime can be attributed to photo-induced electron transfer from the BDT core to the $[Co^{II}(TPY)_2]^{2+}$ unit. To assess the feasibility of photocatalytic CO_2 reduction reactions, we performed Mott–Schottky analysis to examine the band structure of TPY-BDT OG and Co-TPY-BDT CPG at frequencies of 1000, 1500, and 2000 Hz in a 0.5 M Na_2SO_4 electrolyte at pH 7. The analysis showed that both catalysts displayed n-type semiconducting behaviour with a positive slope.[48] The flat band potentials (V_{fb}) were found to be −0.59 V and −0.76 V *versus* NHE (at pH = 7) for Co-TPY-BDT CPG (Fig. S13a†) and TPY-BDT OG (Fig. S13b†), respectively. Based on the bandgaps obtained from UV-Vis absorption spectra, we have elucidated the band diagram, which showed that both TPY-BDT OG and Co-TPY-BDT CPG can be utilized for the photocatalytic CO_2RR (Fig. 3A). Next, DFT calculations were performed to investigate electron transfer feasibility from the light-harvesting BDT unit to the catalytically active site, $[Co^{II}(TPY)_2]^{2+}$. The energetically low-lying LUMO of the $[Co^{II}(TPY)_2]^{2+}$ moiety compared to the LUMO of the $BDT(CONH_2)_2$ unit suggested thermodynamic feasibility of photoinduced electron transfer from the BDT unit to the $[Co^{II}(TPY)_2]^{2+}$ catalytic site (Fig. 3B).

Visible-light-driven photocatalytic CO_2 reduction

We measured the CO_2 adsorption isotherm for Co-TPY-BDT CPG at 298 K and found that the CPG exhibited an uptake of approximately 25 cm^3 g^{-1} (Fig. S14†). This high uptake amount might be attributed to the fibrous morphology of the CPG. This

Open Access Article. Published on 27 January 2025. Downloaded on 11/2/2025 12:12:14 PM.
This article is licensed under a Creative Commons Attribution-NonCommercial 3.0 Unported Licence.

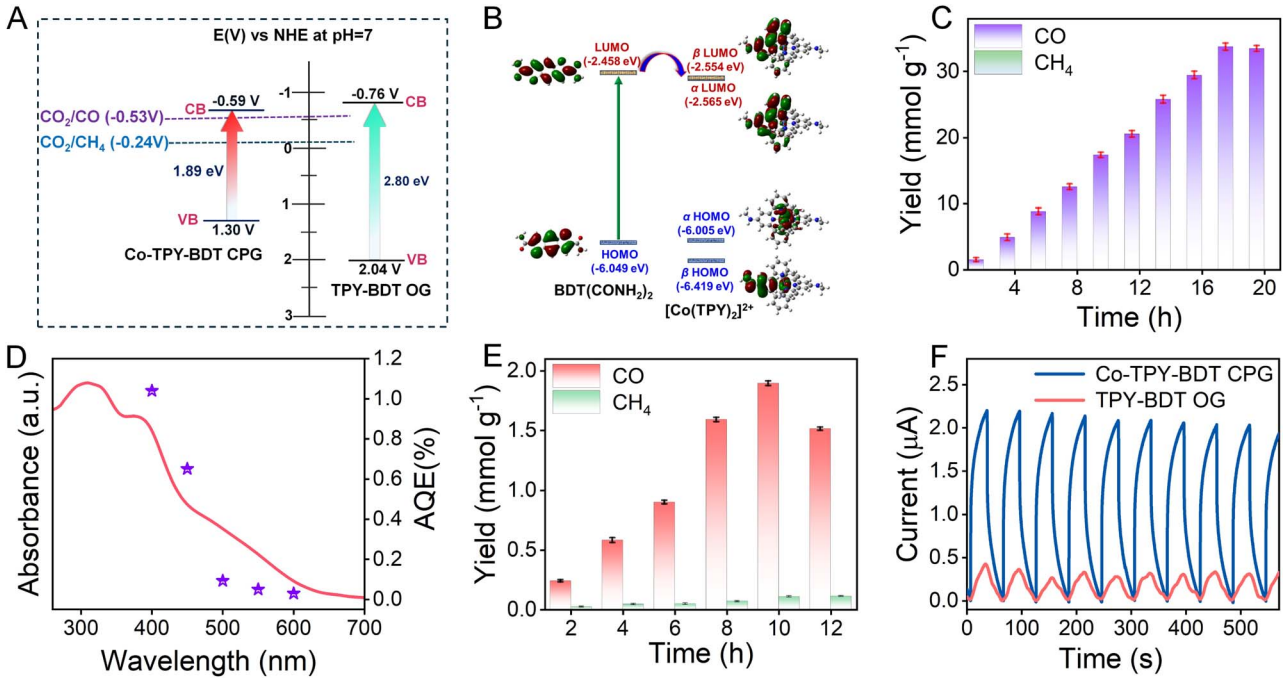

Fig. 3 (A) Band diagrams for TPY-BDT OG and Co-TPY-BDT CPG. (B) HOMO–LUMO energy diagram demonstrating the possibility of electron transfer from $BDT(CONH_2)_2$ to the $[Co(TPY)_2]^{2+}$ moiety in Co-TPY-BDT CPG. (C) The amount profile of CO and CH_4 using the Co-TPY-BDT CPG photocatalyst in the presence of TEA using pure CO_2. (D) Apparent quantum efficiency (AQE) for Co-TPY BDT CPG at various wavelengths during photocatalysis after 6 hours. (E) The amount of CO and CH_4 evolution by Co-TPY-BDT CPG using low-concentration CO_2. (F) Transient photocurrent measurement in 0.5 M Na_2SO_4 at +0.8 V, pH ∼ 7 under visible-light irradiation with a 30-second time interval.

finding implies that the CPG has the potential to efficiently assimilate CO_2, functioning as a promising reservoir for catalytic processes.[49] Photocatalytic CO_2 reduction experiments were performed by exposing a CO_2 (99.99%) saturated acetonitrile (CH_3CN)/water (H_2O) solution to visible light ($\lambda > 400$ nm) from a 300 W xenon lamp (Fig. S15†). The acetonitrile/H_2O combination has been selected due to acetonitrile's superior solubility for CO_2 and the presence of water as a proton source.[50,51] This solution contained 0.5 mg of the Co-TPY-BDT CPG catalyst and 200 μl of TEA, which served as the sacrificial electron donor. The photocatalytic activity was monitored through gas chromatography-mass spectrometry (GC-MS) analysis (Fig. S17†). The photocatalytic CO_2 reduction reactions for Co-TPY-BDT CPG and TPY-BDT OG were both conducted in the xerogel state. The use of the xerogel state of the catalyst facilitated easier handling than the gel state.[21] After several solvent combinations, we identified that a mixture of acetonitrile and water (4 : 1 v/v) with triethylamine (TEA) as a sacrificial electron donor yielded the highest catalytic activity for the Co-TPY-BDT CPG catalyst (Table S4†). Under these conditions, the catalyst achieved a CO evolution of 33.74 mmol g^{-1} with a remarkable selectivity of ∼99% for CO over CH_4 after 18 hours of visible light irradiation (Fig. 3C). The rate of CO production was determined to be 1.9 mmol g^{-1} h^{-1}, with the maximum apparent quantum efficiency recorded at 1.04% at 400 nm (Fig. 3D). The corresponding TON (CO) was calculated to be 32 after 18 h (Fig. S18†). To the best of our knowledge, this catalytic performance is one of the most remarkable achievements in heterogeneous photocatalytic CO_2 reduction to CO under visible light (Table S5†). Furthermore, we explored the visible-light driven photocatalytic CO_2 reduction using TPY-BDT OG under the same conditions as those for Co-TPY-BDT CPG. The TPY-BDT OG exhibited nearly ten times lower activity than the CPG, producing 3.64 mmol g^{-1} of CO over 22 hours with ∼98% selectivity (rate = 165.65 μmol g^{-1} h^{-1}). This highlights the crucial role of the $[Co(TPY)_2]^{2+}$ unit as the predominant active site for CO_2 photoreduction. Furthermore, catalytic experiments with Co-TPY-BDT CPG in the absence of any sacrificial electron donor yielded a negligible CO production (0.073 mmol g^{-1} in 12 h), emphasizing the critical role of a sacrificial electron donor in achieving efficient CO_2 photoreduction. The Co-TPY-BDT CPG photocatalyst demonstrated stable recyclability over five cycles in the presence of TEA (Fig. S19†), maintaining consistent performance without morphological (Fig. S20†) or spectroscopic alterations (Fig. S21†), highlighting its robust stability in the reaction medium. We also conducted photocatalytic reduction of labelled $^{13}CO_2$ (isotopic labelling) using Co-TPY-BDT CPG xerogel to assess the origin of CO in the presence of TEA. GC-MS analysis indicated the exclusive formation of the ^{13}C-labelled product of ^{13}CO, confirming CO_2's role as a substrate in the photocatalysis process (Fig. S22†). The LC-MS analysis of the post-catalytic reaction solution confirms that diethylamine (DEA) and acetaldehyde are the oxidation products of TEA (Fig. S23†). Due to the excellent CO_2 uptake at room temperature and outstanding photoreduction efficiency under pure CO_2

 © 2025 The Author(s). Published by the Royal Society of Chemistry

Open Access Article. Published on 27 January 2025. Downloaded on 11/2/2025 12:12:14 PM.
This article is licensed under a Creative Commons Attribution-NonCommercial 3.0 Unported Licence.

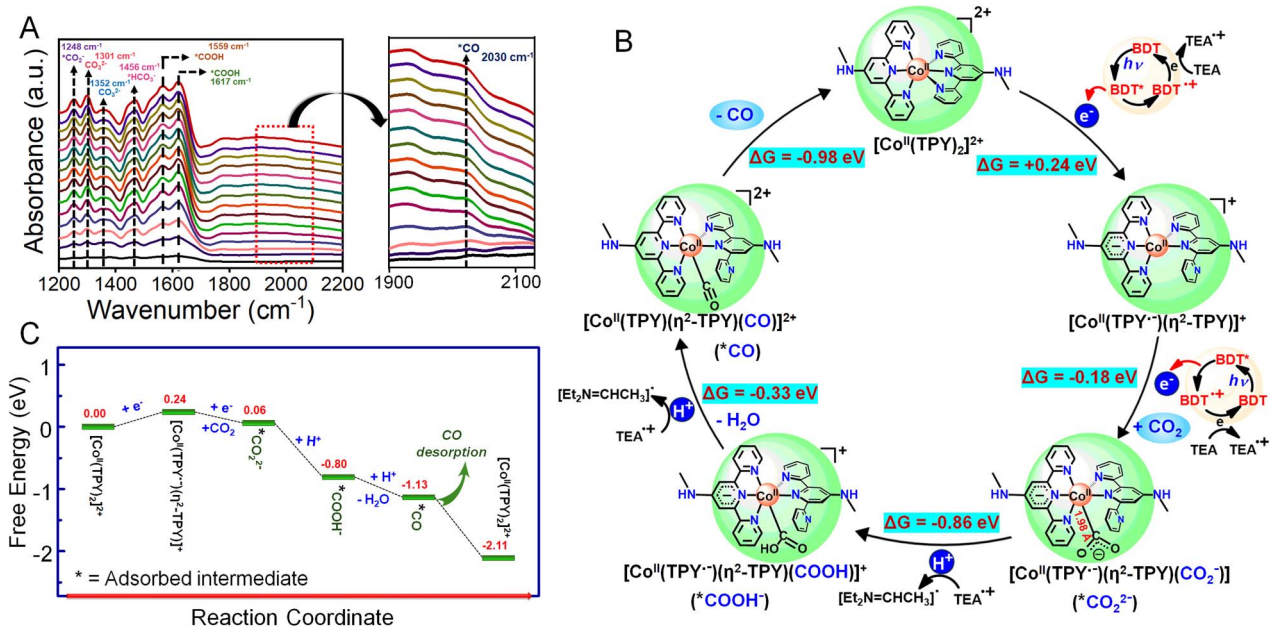

Fig. 4 (A) *In situ* DRIFT spectra of Co-TPY-BDT CPG under visible-light irradiation for CO formation. (B) Proposed mechanism for the reduction of CO_2 to CO utilizing the Co-TPY-BDT CPG catalyst. (C) Relative Gibbs free energy plot.

conditions, combined with the advantageous fibrous morphology of Co-TPY-BDT CPG, we next investigated its performance in reducing low-concentration CO_2.[22,52,53] The fibrous network would likely enhance the efficient diffusion and interaction of CO_2 with the active sites, even in the diluted CO_2 environment. In a 4 : 1 CH_3CN/H_2O solvent with TEA, the catalyst produced 1.9 mmol g^{-1} of CO over 10 h, achieving 94.6% selectivity and a rate of 189.61 μmol g^{-1} h^{-1} (Fig. 3E). These results establish Co-TPY-BDT CPG as one of the most effective catalysts for photocatalytic CO_2 reduction under low-concentration CO_2 conditions (Table S6†). To understand the significant difference in photocatalytic activities between TPY-BDT OG and Co-TPY-BDT CPG, photocurrent measurements were performed under both light and dark conditions. The photocurrent for Co-TPY-BDT CPG in the presence of light was found to be four times higher than that of TPY-BDT OG (Fig. 3F). This result suggests facile charge separation in the case of Co-TPY-BDT CPG under light irradiation due to the presence of Co^{II}. Hence, it is expected to exhibit enhanced photocatalytic activity compared to TPY-BDT OG. These results were further validated through electrochemical impedance spectroscopy (EIS) measurements, where it was found that the charge transfer resistance in Co-TPY-BDT CPG was significantly less than that of TPY-BDT OG under both dark and light-irradiated conditions (Fig. S24†).

Femtosecond transient absorption (fsTA) experiments have been performed to understand the charge transfer dynamics in real time. The early time fsTA data of the BDT ligand (Fig. S25a†) showed a broad absorption band in the range of 550–700 nm and a strong negative signal in the 430–550 nm region. Considering the spectral region of the negative signal which is very similar to the emission spectra of the BDT ligand, it is assigned to stimulated emission (SE) from the photoexcited BDT. The broad positive band is due to the excited state absorption (ESA) of BDT. A similar broad absorption band in the near NIR region is reported for different classes of benzodithiophene molecules.[54,55] Both ESA and SE follow similar multiexponential decay kinetics (Fig. S25b†) with a decay time constant of 1.5 ps (18%), 61 ps (26%), and 425 ps (54%) with a residual long decay of 2%. Unlike BDT, fsTA data of TPY-BDT OG show an ESA band at 550 nm which extends beyond 700 nm (Fig. 5a). The SE band observed in BDT could not be observed in the TPY-BDT OG sample due to the strong fluorescence quenching which is also supported by the steady state emission measurements. The decay kinetics at 500 nm and 640 nm are shown in Fig. 5b. It is evident that the decay of the ESA signal at 640 nm is significantly faster than that in the 500 nm region. This clearly indicates the presence of multiple excited states in these two spectral regions. Since BDT has an ESA band in the 600–700 nm region, we assigned the decay at 640 nm corresponding to the S_1 state of BDT. Following literature reports, the ESA band at 550 nm is assigned to $TPY^{\bullet-}$.[56] The appearance of $TPY^{\bullet-}$ within the instrument response of our setup (0.12 ps), suggests electron transfer from the BDT moiety to the TPY unit in the TPY-BDT OG sample. The fitting of the decay kinetics at 640 nm results in a time constant of 0.5 ps (20%), 23.9 ps (35%), and 405 ps (23%) with a residual decay of ∼23%. Two time constants, 0.5 ps and 23.9 ps, are considerably shorter as compared to the time constant observed for the BDT ligand. Such a shorter time constant is a manifestation of the intramolecular electron transfer from the BDT unit to the TPY unit in the TPY-BDT OG sample. Considering significant overlapping of the ESA bands of BDT and $TPY^{\bullet-}$, the decay time constants for $TPY^{\bullet-}$ were estimated from the decay kinetics at the blue edge

Open Access Article. Published on 27 January 2025. Downloaded on 11/2/2025 12:12:14 PM.
This article is licensed under a Creative Commons Attribution-NonCommercial 3.0 Unported Licence.

of its ESA band (500 nm). From the kinetic trace shown in Fig. 5b, it is evident that $TPY^{\bullet-}$ has a lifetime much longer than the temporal window of our setup (2.5 ns). The kinetic analysis indicates the lifetime of $TPY^{\bullet-}$ is >3 ns. The transient absorption spectra of the Co-TPY-BDT CPG sample are qualitatively very similar to that of the TPY-BDT OG sample as shown in Fig. 5c. However, both the ESA bands due to BDT and $TPY^{\bullet-}$ show some shift with respect to the TPY-BDT OG sample. This small spectral shift might be due to the changes in the intermolecular interaction between coordinating polymer chains. Unlike the TPY-BDT OG sample, the decay of the $TPY^{\bullet-}$ is extremely fast and more than 90% decays within 100 ps. The kinetic analysis of $TPY^{\bullet-}$ decay trace provides time constants of 0.4 ps (74%), 5.7 ps (19%) and 210 ps (7%) with an average lifetime of 16 ps which is more than two orders of magnitude faster than the lifetime observed in the TPY-BDT OG sample (>3 ns). This drastic reduction in the lifetime of $TPY^{\bullet-}$ in the CPG sample is purely due to the presence of cobalt and assigned to the electron transfer from $TPY^{\bullet-}$ to the Co^{II} in the CPG (Fig. 5d). Thus, our fsTA data support efficient electron transfer from the BDT unit to the redox active Co^{II} center of the Co-TPY-BDT CPG catalyst.

We have performed *in situ* diffuse reflectance infrared Fourier transform (DRIFT) spectroscopic study of Co-TPY-BDT CPG to monitor the formation of reaction intermediates during the CO_2 reduction to CO process (Fig. S16†). For background subtraction, we selected FTIR spectra obtained prior to the introduction of CO_2 and without light irradiation. We recorded the spectra at three-minute intervals after introducing CO_2 and water vapour in the presence of visible light. The peak observed at 1248 cm^{-1} corresponds to the stretching frequency of $*CO_2^-$.[57] The peaks at 1456 cm^{-1} can be attributed to the symmetric stretching of $*HCO_3^-$, while the peaks at 1301 and 1352 cm^{-1} correspond to CO_3^{2-}.[22,58,59] The appearance of two peaks at 1559 and 1617 cm^{-1} is attributed to the *COOH intermediate.[60,61] A substantial peak associated with *CO is observed at 2030 cm^{-1}, with its intensity increasing over time, suggesting the accumulation of *CO (Fig. 4a).[17]

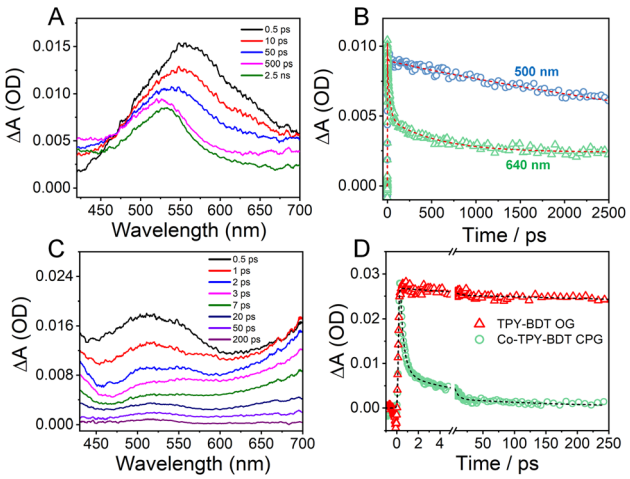

Fig. 5 (A) Transient absorption spectra of TPY-BDT OG dispersed in ethylene glycol at different time delays. (B) The decay kinetics at 500 nm and 640 nm. The line between the data points is the fitted kinetic data. (C) Transient absorption spectra of Co-TPY-BDT CPG in ethylene glycol at different time delays. (D) A comparison of the decay kinetics for TPY-BDT OG and Co-TPY-BDT CPG at 500 nm. The dashed lines are fitted kinetic data.

Furthermore, the mechanism of photocatalytic CO_2 to CO reduction using the Co-TPY-BDT CPG catalyst was investigated *via* DFT calculations based on the intermediates detected during *in situ* DRIFT study.[21,22,38,47,62,63] The proposed catalytic cycle and corresponding Gibbs free energy plot are shown in Fig. 4. For mechanistic investigation, the $[Co^{II}(TPY)_2]^{2+}$ unit was considered the initial catalyst (Fig. S27(iv)†). The BDT unit, upon photoexcitation, would transfer an electron to the catalytic site through an oxidative quenching pathway. The oxidized $BDT^{\bullet+}$ generated in this process would undergo reduction by sacrificial agent TEA to recover BDT (Fig. 4b). During the catalysis, the initial catalyst $[Co^{II}(TPY)_2]^{2+}$ would undergo one-electron reduction to generate $[Co^{II}(TPY^{\bullet-})(\eta^2\text{-}TPY)]^+$, which is an uphill process (ΔG = +0.24 eV). In the next step, $[Co^{II}(TPY^{\bullet-})(\eta^2\text{-}TPY)]^+$ would engage in another electron reduction followed by the oxidative addition of CO_2 to generate $[Co^{II}(TPY^{\bullet-})(\eta^2\text{-}TPY)(CO_2^-)]$ or $*CO_2^{2-}$ (ΔG = −0.18 eV), which after protonation would afford intermediate $[Co^{II}(TPY^{\bullet-})(\eta^2\text{-}TPY)(COOH)]^+$ or $*COOH^-$ (ΔG = −0.86 eV).[64] The two-electron reduction of the catalyst prior to CO_2-binding would facilitate the CO_2 oxidative addition process, leading to stronger CO_2-binding as compared to the CO_2-binding after one-electron reduction.[62,63] More electron-rich $[Co^{I}(L^-)]^{2-}$ (where, L = ligand) species (two-electron reduced catalyst) has higher nucleophilicity for CO_2 activation than the one-electron reduced $[Co^{II}(L^-)]^-$ species.[65,66] Next, the protonation followed by water elimination from $[Co^{II}(TPY^{\bullet-})(\eta^2\text{-}TPY)(COOH)]^+$ or $*COOH^-$ would generate $[Co^{II}(TPY)(\eta^2\text{-}TPY)(CO)]^{2+}$ or *CO intermediate in an exergonic process (ΔG = −0.33 eV). Lastly, $[Co^{II}(TPY)(\eta^2\text{-}TPY)(CO)]^{2+}$ or *CO intermediate would regenerate the initial catalyst $[Co^{II}(TPY)_2]^{2+}$ with rapid CO desorption, which is a highly exergonic step (ΔG = −0.98 eV) (Fig. 4b and c). Notably, the initial $[Co^{II}(TPY)_2]^{2+}$ to $[Co^{II}(TPY^{\bullet-})(\eta^2\text{-}TPY)]^+$ conversion step was found to be the only uphill process (ΔG = +0.24 eV) of the whole catalytic cycle, which suggests it as the rate-determining step (rds) (Fig. 4c). In addition, the more exergonic CO desorption step from $[Co^{II}(TPY)(\eta^2\text{-}TPY)(CO)]^{2+}$ or *CO intermediate (ΔG = −0.98 eV), compared to its further reduction to $[Co^{II}(TPY)(\eta^2\text{-}TPY)(CHO)]^{2+}$ or *CHO (ΔG = −0.75 eV), justifies high CO product selectivity over CH_4 (Fig. S26†).

Conclusions

We have introduced a successful design strategy and synthesis of a metal–organic 'soft' coordination polymer gel, incorporating both light-absorbing chromophores and active catalytic centers in the same units. This innovative approach enables visible-light-driven CO_2 reduction to CO with an impressive selectivity of ∼99%. In the presence of TEA as a sacrificial electron donor, the Co-TPY-BDT CPG photocatalyst achieved a maximum CO yield of 33.74 mmol g^{-1} in 18 h, with an activity rate of 1.9 mmol g^{-1} h^{-1}. Among the reported heterogeneous photocatalytic CO_2RR, these values stand out as remarkable,

 © 2025 The Author(s). Published by the Royal Society of Chemistry

Open Access Article. Published on 27 January 2025. Downloaded on 11/2/2025 12:12:14 PM.
This article is licensed under a Creative Commons Attribution-NonCommercial 3.0 Unported Licence.

achieved under visible light conditions by the emerging class of CPG–based materials. Furthermore, our study involved the low-concentration CO_2RR utilizing Co-TPY-BDT CPG and was particularly intriguing from an energy-saving standpoint. This indicates that the catalyst does not require a concentrated form of gas mixtures and can be used directly to reduce CO_2 under low partial pressures. *In situ* DRIFTS and DFT calculations revealed mechanistic insights into the CO_2 reduction pathways. Moreover, femtosecond transient absorption spectroscopy confirmed the electron transfer pathway from the BDT core to the $[Co(TPY)_2]^{2+}$ complex within the Co-TPY-BDT CPG. These findings open a completely unexplored frontier for the development of a scalable and efficient 'soft' material-based photocatalyst and offer an achievable way of utilising solar energy for the reduction of CO_2.

Data availability

All associated data are included in the ESI.†

Author contributions

S. M. and T. K. M. designed the concept of this work. S. M. performed all the major experiments. S. N. performed the TA experiment. S. M., F. A. R., T. N. D., S. N. and T. K. M. analysed all the experimental data. F. A. R. conducted all the computational study. S. M., F. A. R., S. N. and T. K. M. wrote the manuscript. T. N. D. made the TOC and schematic. All authors discussed the results and commented on the manuscript.

Conflicts of interest

There are no conflicts to declare.

Acknowledgements

S. M. and F. A. R. acknowledge the Council of Scientific and Industrial Research (CSIR), Govt. of India, for the fellowship. T. N. D. acknowledges JNCASR for a graduate research fellowship. T. K. M. acknowledges SERB, Dept. of Science and Technology (DST), Govt. of India, for financial support (project no. SPR/2021/000592). The authors acknowledge the support and resources provided by the "PARAM Yukti Facility" under the National Supercomputing Mission, Government of India, at JNCASR, Bangalore. SAMat, ICMS, SSL research facility and the Sheikh Saqr senior fellowship (T. K. M.) are also gratefully acknowledged.

References

1 M. Reichstein, M. Bahn, P. Ciais, D. Frank, M. D. Mahecha, S. I. Seneviratne, J. Zscheischler, C. Beer, N. Buchmann and D. C. Frank, *Nature*, 2013, **500**, 287–295.
2 C. Su, Z. Chen, Q. Feng, F. Wei, M. Zhang, A. Mo, H.-H. Huang, H. Hu and D. Liu, *Inorg. Chem.*, 2022, **61**, 19748–19755.
3 F. Zhao, J. Bae, X. Zhou, Y. Guo and G. Yu, *Adv. Mater.*, 2018, **30**, 1801796.
4 J. Barber and P. D. Tran, *J. R. Soc. Interface*, 2013, **10**, 20120984.
5 A. Cho, *Science*, 2010, **329**, 786–787.
6 Z. Tang, S. Xu, N. Yin, Y. Yang, Q. Deng, J. Shen, X. Zhang, T. Wang, H. He and X. Lin, *Adv. Mater.*, 2023, **35**, 2210693.
7 S. J. Davis, K. Caldeira and H. D. Matthews, *Science*, 2010, **329**, 1330–1333.
8 O. Dumele, L. Đorđević, H. Sai, T. J. Cotey, M. H. Sangji, K. Sato, A. J. Dannenhoffer and S. I. Stupp, *J. Am. Chem. Soc.*, 2022, **144**, 3127–3136.
9 S. R. V. Parambil, S. Karmakar, F. A. Rahimi and T. K. Maji, *ACS Appl. Mater. Interfaces*, 2023, **15**, 27821–27831.
10 S. Navalón, A. Dhakshinamoorthy, M. Álvaro and H. Garcia, *ChemSusChem*, 2013, **6**, 562–577.
11 S. C. Yan, S. X. Ouyang, J. Gao, M. Yang, J. Y. Feng, X. X. Fan, L. J. Wan, Z. S. Li, J. H. Ye and Y. Zhou, *Angew. Chem.*, 2010, **36**, 6544–6548.
12 A. Dhakshinamoorthy, S. Navalon, A. Corma and H. Garcia, *Energy Environ. Sci.*, 2012, **5**, 9217–9233.
13 J. Zhou, W. Chen, C. Sun, L. Han, C. Qin, M. Chen, X. Wang, E. Wang and Z. Su, *ACS Appl. Mater. Interfaces*, 2017, **9**, 11689–11695.
14 S. Karmakar, S. Barman, F. A. Rahimi and T. K. Maji, *Energy Environ. Sci.*, 2021, **14**, 2429–2440.
15 S. R. V. Parambil, F. A. Rahimi, R. Ghosh, S. Nath and T. K. Maji, *Inorg. Chem.*, 2023, **62**, 19312–19322.
16 S. Karmakar, S. Barman, F. A. Rahimi, D. Rambabu, S. Nath and T. K. Maji, *Nat. Commun.*, 2023, **14**, 4508.
17 A. Dey, J. Pradhan, S. Biswas, F. Ahamed Rahimi, K. Biswas and T. K. Maji, *Angew. Chem.*, 2024, **136**, e202315596.
18 A. Dey, F. A. Rahimi, S. Barman, A. Hazra and T. K. Maji, *J. Mater. Chem. A*, 2023, **11**, 13615–13622.
19 Z. He, J. Goulas, E. Parker, Y. Sun, X.-d. Zhou and L. Fei, *Catal. Today*, 2023, **409**, 103–118.
20 S. Biswas, A. Dey, F. A. Rahimi, S. Barman and T. K. Maji, *ACS Catal.*, 2023, **13**, 5926–5937.
21 P. Verma, F. A. Rahimi, D. Samanta, A. Kundu, J. Dasgupta and T. K. Maji, *Angew. Chem., Int. Ed.*, 2022, **61**, e202116094.
22 P. Verma, A. Singh, F. A. Rahimi, P. Sarkar, S. Nath, S. K. Pati and T. K. Maji, *Nat. Commun.*, 2021, **12**, 7313.
23 Y. Fang, T. Liu, L. Chen and D. Chao, *ACS Catal.*, 2023, **13**, 2086–2093.
24 P. Sutar and T. K. Maji, *Chem. Commun.*, 2016, **52**, 8055–8074.
25 P. Sutar and T. K. Maji, *Dalton Trans.*, 2020, **49**, 7658–7672.
26 P. Sutar and T. K. Maji, *Inorg. Chem.*, 2017, **56**, 9417–9425.
27 Y. Huo, Z. He, C. Wang, L. Zhang, Q. Xuan, S. Wei, Y. Wang, D. Pan, B. Dong and R. Wei, *Chem. Commun.*, 2021, **57**, 1413–1429.
28 H. Wu, J. Zheng, A. L. Kjøniksen, W. Wang, Y. Zhang and J. Ma, *Adv. Mater.*, 2019, **31**, 1806204.
29 A. J. Savyasachi, O. Kotova, S. Shanmugaraju, S. J. Bradberry, G. M. Ó'Máille and T. Gunnlaugsson, *Chem*, 2017, **3**, 764–811.

Open Access Article. Published on 27 January 2025. Downloaded on 11/2/2025 12:12:14 PM.
This article is licensed under a Creative Commons Attribution-NonCommercial 3.0 Unported Licence.

30 J. H. Kim, D. H. Nam, Y. W. Lee, Y. S. Nam and C. B. Park, *Small*, 2014, **10**, 1272–1277.
31 T. Christoff-Tempesta, A. J. Lew and J. H. Ortony, *Gels*, 2018, **4**, 40.
32 M. Gao, C. K. Peh, L. Zhu, G. Yilmaz and G. W. Ho, *Adv. Energy Mater.*, 2020, **10**, 2000925.
33 M. Li, W. Ni, X. Wan, Q. Zhang, B. Kan and Y. Chen, *J. Mater. Chem. A*, 2015, **3**, 4765–4776.
34 X. Yin, Q. An, J. Yu, F. Guo, Y. Geng, L. Bian, Z. Xu, B. Zhou, L. Xie and F. Zhang, *Sci. Rep.*, 2016, **6**, 25355.
35 C. An and J. Hou, *Acc. Mater. Res.*, 2022, **3**, 540–551.
36 M. F. Kuehnel, K. L. Orchard, K. E. Dalle and E. Reisner, *J. Am. Chem. Soc.*, 2017, **139**, 7217–7223.
37 L. Chen, Y. Wu, Y. Hu and D. Chao, *J. CO2 Util.*, 2022, **62**, 102083.
38 J. J. Leung, J. Warnan, K. H. Ly, N. Heidary, D. H. Nam, M. F. Kuehnel and E. Reisner, *Nat. Catal.*, 2019, **2**, 354–365.
39 S. S. Bagde, H. Park, S.-M. Lee and S.-H. Lee, *New J. Chem.*, 2016, **40**, 2063–2070.
40 S. Ghosh, F. Steinke, A. Rana and S. Biswas, *Inorg. Chem. Front.*, 2022, **9**, 859–869.
41 E. D. Holt, J. Wang, R. W. Winkel, M. Younus and K. S. Schanze, *J. Photochem. Photobiol.*, 2021, **8**, 100060.
42 P. Gao, D. Beckmann, H. N. Tsao, X. Feng, V. Enkelmann, W. Pisula and K. Müllen, *Chem. Commun.*, 2008, 1548–1550.
43 J. W. Wang, H. H. Huang, J. K. Sun, T. Ouyang, D. C. Zhong and T. B. Lu, *ChemSusChem*, 2018, **11**, 1025–1031.
44 E. Boutin, L. Merakeb, B. Ma, B. Boudy, M. Wang, J. Bonin, E. Anxolabéhère-Mallart and M. Robert, *Chem. Soc. Rev.*, 2020, **49**, 5772–5809.
45 B. S. Luisi, K. D. Rowland and B. Moulton, *Chem. Commun.*, 2007, 2802–2804.
46 N. Fukaya, S. Ogi, H. Sotome, K. J. Fujimoto, T. Yanai, N. Bäumer, G. Fernández, H. Miyasaka and S. Yamaguchi, *J. Am. Chem. Soc.*, 2022, **144**, 22479–22492.
47 D. Kim, S. Bhattacharjee, E. Lam, C. Casadevall, S. Rodríguez-Jiménez and E. Reisner, *Small*, 2024, 2400057.
48 J.-S. Qin, S. Yuan, L. Zhang, B. Li, D.-Y. Du, N. Huang, W. Guan, H. F. Drake, J. Pang and Y.-Q. Lan, *J. Am. Chem. Soc.*, 2019, **141**, 2054–2060.
49 Z. Fu, X. Wang, A. M. Gardner, X. Wang, S. Y. Chong, G. Neri, A. J. Cowan, L. Liu, X. Li and A. Vogel, *Chem. Sci.*, 2020, **11**, 543–550.
50 S. Piontek, K. junge Puring, D. Siegmund, M. Smialkowski, I. Sinev, D. Tetzlaff, B. R. Cuenya and U.-P. Apfel, *Chem. Sci.*, 2019, **10**, 1075–1081.
51 Y. Tomita, S. Teruya, O. Koga and Y. Hori, *J. Electrochem. Soc.*, 2000, **147**, 4164.
52 T. Kajiwara, M. Fujii, M. Tsujimoto, K. Kobayashi, M. Higuchi, K. Tanaka and S. Kitagawa, *Angew. Chem., Int. Ed.*, 2016, **55**, 2697–2700.
53 P. Chen, L. Blaney, G. Cagnetta, J. Huang, B. Wang, Y. Wang, S. Deng and G. Yu, *Environ. Sci. Technol.*, 2019, **53**, 1564–1575.
54 S. Sharma, Z. Wei, F. C. Grozema and S. Sengupta, *Phys. Chem. Chem. Phys.*, 2020, **22**, 25514–25521.
55 J. Cheng, W. Wang, J. Zhang, S. Wan, B. Cheng, J. Yu and S. Cao, *Angew. Chem.*, 2024, e202406310.
56 V. Grosshenny, A. Harriman and R. Ziessel, *Angew. Chem., Int. Ed.*, 1996, **34**, 2705–2708.
57 L. Liu, H. Zhao, J. M. Andino and Y. Li, *ACS Catal.*, 2012, **2**, 1817–1828.
58 L. Liu and Y. Li, *Aerosol Air Qual. Res.*, 2014, **14**, 453–469.
59 W. Wang, D. Xu, B. Cheng, J. Yu and C. Jiang, *J. Mater. Chem. A*, 2017, **5**, 5020–5029.
60 L. Liang, X. Li, Y. Sun, Y. Tan, X. Jiao, H. Ju, Z. Qi, J. Zhu and Y. Xie, *Joule*, 2018, **2**, 1004–1016.
61 X. Li, Y. Sun, J. Xu, Y. Shao, J. Wu, X. Xu, Y. Pan, H. Ju, J. Zhu and Y. Xie, *Nat. Energy*, 2019, **4**, 690–699.
62 N. Elgrishi, M. B. Chambers, V. Artero and M. Fontecave, *Phys. Chem. Chem. Phys.*, 2014, **16**, 13635–13644.
63 N. Elgrishi, M. B. Chambers and M. Fontecave, *Chem. Sci.*, 2015, **6**, 2522–2531.
64 A. Bairagi, A. Y. Pereverzev, P. Tinnemans, E. A. Pidko and J. Roithová, *J. Am. Chem. Soc.*, 2024, **146**, 5480–5492.
65 T. W. Schneider, M. Z. Ertem, J. T. Muckerman and A. M. Angeles-Boza, *ACS Catal.*, 2016, **6**, 5473–5481.
66 F. A. Rahimi, S. Dey, P. Verma and T. K. Maji, *ACS Catal.*, 2023, **13**, 5969–5978.

 © 2025 The Author(s). Published by the Royal Society of Chemistry